JGR Space Physics

RESEARCH ARTICLE
10.1029/2022JA030572

The Global Monsoon Convective System as Reflected in Upper Atmosphere Gravity Waves

Jeffrey M. Forbes[1], Manfred Ern[2], and Xiaoli Zhang[1]

[1]Ann and H.J. Smead Department of Aerospace Engineering Sciences, University of Colorado, Boulder, CO, USA, [2]Institute of Energy and Climate Research – Stratosphere (IEK-7), Forschungszentrum Jülich GmbH, Jülich, Germany

Key Points:

- The Global Monsoon Convective System (GMCS) is defined in terms of annual range (AR = |DJF − JJA|/(DJF − JJA)) of Outgoing Longwave Radiation (OLR) in six tropical geographic regions
- The extended GMCS is examined in terms of gravity wave momentum fluxes (GWMFs) at 30, 50, 70, and 90 km, and their relation to source (OLR) variability, MERRA2 and HWM14 winds
- Intermonthly variability of GWMFs are quantified in terms of OLR, local Doppler-shifting, 15-km wind filtering, and instrument sensitivity

Supporting Information:

Supporting Information may be found in the online version of this article.

Correspondence to:

J. M. Forbes,
forbes@colorado.edu

Citation:

Forbes, J. M., Ern, M., & Zhang, X. (2022). The global monsoon convective system as reflected in upper atmosphere gravity waves. *Journal of Geophysical Research: Space Physics*, *127*, e2022JA030572. https://doi.org/10.1029/2022JA030572

Received 19 APR 2022
Accepted 10 AUG 2022

Abstract The concept of a global monsoon system collectively comprising 6 tropical regions is applied to Outgoing Longwave Radiation (OLR) as a proxy for convectively generated gravity waves (GWs), leading to the global monsoon *convective* system (GMCS). The six tropical regions are North and South Africa, Central and South America, and the South Asia-Pacific and Malay Archipelago/Australia-Pacific regions. The *extended* GMCS is considered in terms of gravity wave momentum fluxes (GWMFs) at 30, 50, 70, and 90 km altitude during the summer season in both hemispheres between December 2016, and August 2020. The GWMFs are inferred from TIMED/SABER temperature measurements. Intermonthly, interseasonal, and interannual variations in monthly mean GWMFs are interpreted in terms of OLR as a proxy for the spatial-temporal variability of GW sources, and in terms of MERRA2 zonal winds that quantify the influences of changes in background propagation conditions. It is found that temporal variations in GWMFs associated with the GMCS as a whole are not highly correlated with OLR, but at 30, 50, and 70 km are quantitatively linked to Doppler-shifting effects by local winds, wind filtering at 15 km altitude, and "instrument filtering." These effects are also compared and examined in the context of GW variances at 50 km in Southern Hemisphere summer measured by the CIPS instrument on the AIM satellite, which measures a different part of the GW spectrum. The SABER GWMF response at 90 km is irregular and variable, but sometimes consists of 3- and 4-peaked structures in longitude that may reflect nonmigrating tide influences on GW propagation conditions.

1. Introduction

Broadly speaking, the Global Monsoon System (GMS) is the tropical response of the coupled atmosphere-land-ocean-cryosphere-biosphere system to the annual variation of solar radiative forcing (e.g., see review by Wang et al. [2011], and references therein). Associated with this solar-driven divergent circulation (Trenberth et al., 2000) that is modulated by land-sea differences are "wet summer" and "dry winter" seasons that migrate between the hemispheres. Consequently, given the availability of satellite-based global measurements of precipitation, rainfall rates (RR) are often used to quantify the latitude-longitude and seasonal distribution of the GMS, either through the use of empirical orthogonal functions or by depicting the "annual range (AR)" of precipitation in some way. AR refers to the local summer-minus-winter precipitation, that is, June-July-August (JJA) minus December-January-February (DJF) precipitation in the Northern Hemisphere (NH) and DJF minus JJA in the Southern Hemisphere (SH).

Also contained within the GMS, and closely associated with high RR, are regions of intense convection, updrafts, and latent heating that serve as excitation sources for gravity waves (GW). In this paper, we apply the concept of AR to satellite-based measurements of outgoing long-wave radiation (OLR) to delineate the global distribution and variability of convectively generated GWs associated with the GMS as a whole. The major focus is to explore the vertical extension of the GMS to higher altitudes in the form of GWs, including the effects of filtering and Doppler-shifting of the GWs by the background wind field. GW responses at 30 km, 50 km, 70 km, and 90 km altitude are in the form of GW momentum fluxes (GWMFs) estimated from limb temperature measurements during 2016–2020 made by the Sounding of the Atmosphere using Broadband Emission Radiometry (SABER) instrument on the Thermosphere Ionosphere Mesosphere Energetics and Dynamics (TIMED) satellite (Ern et al., 2011, 2018). The time period is specifically chosen to overlap with measurements of convectively forced GWs from the Cloud Imaging and Particle Size (CIPS) instrument on the Aeronomy of Ice in the Mesosphere (AIM) satellite (Randall et al., 2017) at 50 km altitude. The CIPS/AIM measurements were the focus of a similar study by Forbes et al. (2021), which, however, is confined to the SH and involves a different scale of GWs than those considered here.

The wider importance of better understanding vertical coupling due to convectively generated GWs rests in the fact that convectively generated GWs represent an effective means of redistributing energy, momentum, and variability throughout the atmosphere, even to satellite altitudes (H. Liu et al., 2017; H.-L. Liu et al., 2014, Park et al., 2014; Trinh et al., 2018; Vadas & Liu, 2009; Vadas et al., 2014; Yiğit & Medvedev, 2015; Yiğit et al., 2009). A number of prior works have derived GW-related properties in the stratosphere and/or mesosphere from satellite-based data and made connections with convective GW sources using OLR as a proxy (e.g., Ern et al., 2011, 2017, 2018; Fetzer & Gille, 1994; Hoffmann et al., 2013; Jiang et al., 2004; McLandress et al., 2000; Wright & Gille, 2011; Wu & Waters, 1996; to name just a few representative examples). These studies mainly focused on seasonal averages, and often did not quantify source-response relationships. The distinguishing features of the present study are that we explore the global GW response to the GMS at several altitudes within the middle atmosphere, with particular focus on intermonthly and interannual variability, and include the role of background winds on the nature of the response.

The following three sections, respectively, briefly summarize the data used for the present study; demonstrate how the GMS is manifested in the stratosphere, mesosphere, and lower thermosphere in terms of GWMFs; and quantify the observed GWMF variability in terms of variability in OLR and background winds between the source and the altitude of observation. Section 5 provides a brief summary and conclusions.

2. SABER GW Measurements and Auxiliary Data

SABER is an infrared (IR) limb sounder that was launched into a 625 km 73° inclination orbit on the TIMED satellite on 7 December 2001, and is still acquiring data. Among other parameters, SABER provides temperature-pressure profiles of the atmosphere from approximately 20–110 km altitude based on the 15 μm emission of CO_2. SABER views the atmosphere at 90° to the satellite velocity vector, so that latitude coverage on a given day extends from about 50° latitude in one hemisphere to 82° in the other. This viewing geometry alternates once every 60 days due to 180° yaw maneuvers such that latitudes within ±50° are covered continuously at 30 longitudes per day if ascending and descending orbit legs are both considered. The methodology for deriving gravity wave parameters including GWMFs from SABER measurements is described in Ern et al. (2004, 2011, 2018). SABER measurements are only sensitive to GWs with $\lambda_H \gtrsim$ 100–200 km and λ_z in the range ~4–25 km. The uncertainty in λ_H and lower-end value of 100 km pertains to the shorter-scale waves that propagate obliquely to the satellite path, and that project as longer-scale waves in the measurements. The uncertainty in λ_H leads to at least a factor of 2 uncertainty in GWMF. The GWMFs are calculated within 20° × 30° latitude × longitude bins, each bin slid 5° in latitude and 10° in longitude to yield a final 5° × 10° latitude × longitude grid. Calculations of GW parameters such as temperature variances, temperature squared amplitudes, and potential energy per unit mass were also possible using smaller (10° × 15°) bins and a finer (2.5° × 5°) grid, but differences in their spatial distributions from those of GWMFs were not sufficiently different to warrant their use in the analysis, rather than the more physically relevant GWMF.

3. Manifestations of the GMS From the Troposphere to the Mesopause (ca. 90 km)

Although the global monsoon system is more commonly delineated in terms of RR, we have chosen here to delineate the global monsoon *convective* system (GMCS) in terms of OLR under the assumption that OLR is more indicative of deep convective sources of GWs (Jia et al., 2014). Figure 1a depicts the AR of the GMCS in terms of OLR (Liebmann & Smith, 1996), where we define the AR to be (JJA-DJF)/(JJA + DJF) in the NH, and (DJF-JJA)/(JJA + DJF) in the SH. The data analyzed extend from December 2016, through August 2020. Note that lower OLR (colder cloud top temperatures) correspond to more vigorous convection (and presumably more intense GW generation), and to darker red hew in the color scale. For later quantitative analysis, six regions of enhanced convective activity are indicated by the boxed regions and include North and South Africa (NAf and SAf), Central and South America (CAm and SAm), the South Asia-Pacific (SAP) region, and the Malay Archipelago/Australia-Pacific (MAP) region. The latitude × longitude boundaries of these boxes are provided in Table S1 of Supporting Information S1, and were arrived at by objective visual analysis with the goal of defining areas wherein the mean OLR values would be representative of the interannual, intraannual, and geographical variations of GW source intensity attached to each one.

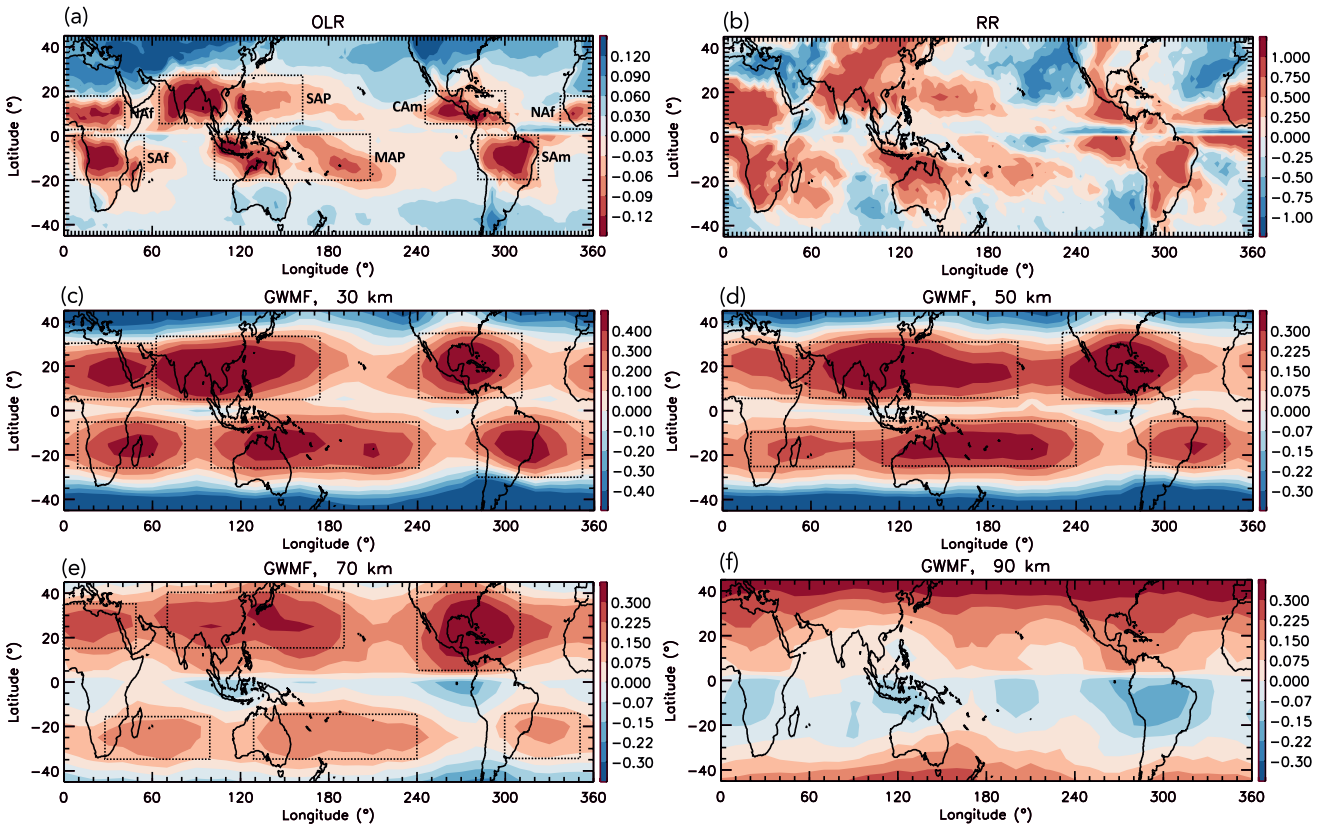

Figure 1. Annual Range (AR) as defined in the text for (a) OLR, (b) RR, and (c–f) GWMF at 30, 50, 70, and 90 km, respectively. The six convective regions are identified for the purposes of this paper as North and South Africa (NAf and SAf), Central and South America (CAm and SAm), the South Asia-Pacific (SAP) region, and the Malay Archipelago/Australia-Pacific (MAP) region. The dashed-line boxes correspond to latitude × longitude regions over which average values of OLR or GWMF are defined that represent amplitudes of GW "sources" and "responses", respectively, for use in quantitative analysis of source-response relationships.

Figure 1b illustrates AR defined in the same way, except for RR from the Global Precipitation Measurement Mission (GPMM, Huffman et al., 2014). The RR distributions are not as localized and well-defined as OLR, since they do not distinguish the monsoon climate from arid and semiarid or Mediterranean climate regimes, or from equatorial perennial rainfall Wang et al. (2011). Additional restrictions can be placed on the AR values for RR to tighten and better define the monsoon precipitation domain (e.g., J. Liu et al., 2009; Wang & Ding, 2006; Wang et al., 2011). However, such additional restrictions do not appear to be necessary for OLR.

Figures 1c–1f depict the AR for gravity wave momentum flux (GWMF) estimates derived from the SABER temperature data as described by Ern et al. (2011, 2018), for altitudes of 30, 50, 70, and 90 km, respectively. These latitude × longitude distributions do not differ appreciably from those based on temperature variance, T^2, or potential energy (not shown). The GWMF distributions at 30, 50, and 70 km also include boxed regions wherein average values can be defined that represent the GW "responses" corresponding to the mean "source" regions depicted in Figure 1a, for later quantitative analysis of source-response relationships. The latitude × longitude boundaries of these boxes are also listed in Table S1 of Supporting Information S1 along with those of OLR, and were defined keeping in mind that some slight latitude-longitude movement of the GWMF response regions occurred from month to month.

At 30 km (Figure 1c), the latitude × longitude distributions of GWMF mirror those of OLR, except are broadened zonally and meridionally with respect to the source distributions, a natural result of oblique GW propagation and the latitude × longitude resolution of the GWMFs. Note that the elongated GWMF structures in the Indo-Pacific region suggest a connection with both the land-mass and oceanic components of the SAP and MAP regions designated in Figure 1a, and this is why the boxed "source" regions have been defined as such. If the oceanic regions were not a significant source of GWs, then it is supposed that the longitudinal structures would look more like the CAm/SAm pair. A similar connection to an oceanic convective source is indicated in the CIPS GW variances at

50 km in the SH monsoon study by Forbes et al. (2021; see their Figure 1), designated there as the South Pacific Convergence Zone (SPCZ).

The GWMFs at 30 km are shifted poleward with respect to the source regions identified in Figure 1a. The 50 and 70 km GWMF distributions in Figures 1d and 1e mirror those at 30 km and are shifted further poleward. The poleward shift of GW signatures with respect to convective source regions has been noted in other datasets and ray tracing studies (e.g., Chen et al., 2019; Choi et al., 2009; Forbes et al., 2021; Jiang et al., 2004; Kalisch et al., 2014; McLandress et al., 2000; Sato et al., 2009; Thurairajah et al., 2017; Trinh et al., 2016; Yasui et al., 2016). The broad consensus of these authors is that waves launched from tropical convective sources follow a slanted propagation path formed by westward winds of the summer midlatitude jet that increase with height and latitude, Doppler-shifting them to longer vertical wavelengths, increased intrinsic frequencies and phase speeds, and larger saturation amplitudes. In specific terms, meridional wind gradients can refract GW horizontal wavenumber vectors such that their meridional component strengthens (Preusse et al., 2009; Sato et al., 2009). At the same time, the appearance of GWs at any given background wind speed is modulated by the observational limits of the particular instrument at hand, which may increase or decrease their observability. The term "observational filter" was coined by Alexander (1998; see also Alexander et al., 2010) to describe this effect. Choi et al. (2009) and Preusse et al. (2009) also suggest that the poleward spread of GWs may also be affected by their launch direction at the source.

In terms of observability, at this point it is worth mentioning the particular sensitivity of GWMF saturation amplitudes to Doppler-shifting vis-a-vis a power of 3 dependence on vertical wavelength (e.g., Preusse et al., 2006). In the following section, the modulation of GW saturation amplitudes by Doppler-shifting will be invoked to explain the change in correlation between GWMF and local wind speeds between 30, 50, and 70 km altitude. See also Ern et al. (2015) where a similar line of thinking was put forth in the context of the stratopause semiannual oscillation.

Finally, it is noted that the wave-3 GWMF structure between 5° and 35°N at 90 km (Figure 1f) is consistent with the analysis of daily SABER GWMFs during the NH summer of 2007 by Thurairajah et al. (2017), who convincingly demonstrated a similar progressively poleward shift to higher latitudes tied to the easterly summer jet. This wave-3 structure is thus plausibly interpreted in terms of a further poleward shift of the structure at 70 km, although no supporting wind information between 70 and 90 km is available to support this conjecture. What is notably missing at 90 km is the South Asia part of the SAP response that exists at lower altitudes between about 5° and 30°N and 60°–120°E. Examination of GWMFs at 90 km for individual months (see Supporting Information S1) reveals that there exists a minimum in GWMF, variable in its extent and specific location from month to month, within the broad 0° to 30°N and 45°–135°E region, that appears to account for this feature in the AR. At the same time, there is no depletion in GW forcing as reflected in OLR (see Supporting Information S1). This level of spatial and temporal variability that is specific to 90 km suggests a connection with variable propagation conditions. In the SH, there is no clear poleward extension of the SH GWMF wave-3 structure, but instead a 4-peaked structure, well-correlated spatially to the AR in OLR in Figure 1a, but indicating summer DJF-minus-JJA *deficits* in GWMF between the equator and 20°S. The SH latitude-longitude structures also exhibit significant intermonthly and interannual variability compared to 30, 50, and 70 km. These differences from behaviors at lower altitudes suggest that additional factors may be at play at 90 km. Further discussion of GWMFs at 90 km is deferred to Section 5.

4. Quantitative Analysis of GWMF Variability Attached to the GCMS

4.1. SABER GWMF at 30, 50, and 70 km

In keeping with the overall theme of this paper, we now investigate the GW response of the global monsoon convective system *as a whole* to intermonthly, interseasonal, and interannual variability in sources and the propagation environment. In addition to other attributes of OLR over RR noted above, OLR is also chosen as the preferred proxy for GW source distributions since OLR exhibits a better correspondence with distributions of GWMF. For instance, in the vicinity of South America in Figure 1b, where there are 3–4 maxima in RR, there is just one maximum associated with the Brazil-Bolivia region with respect to both OLR and GWMF (i.e., compare

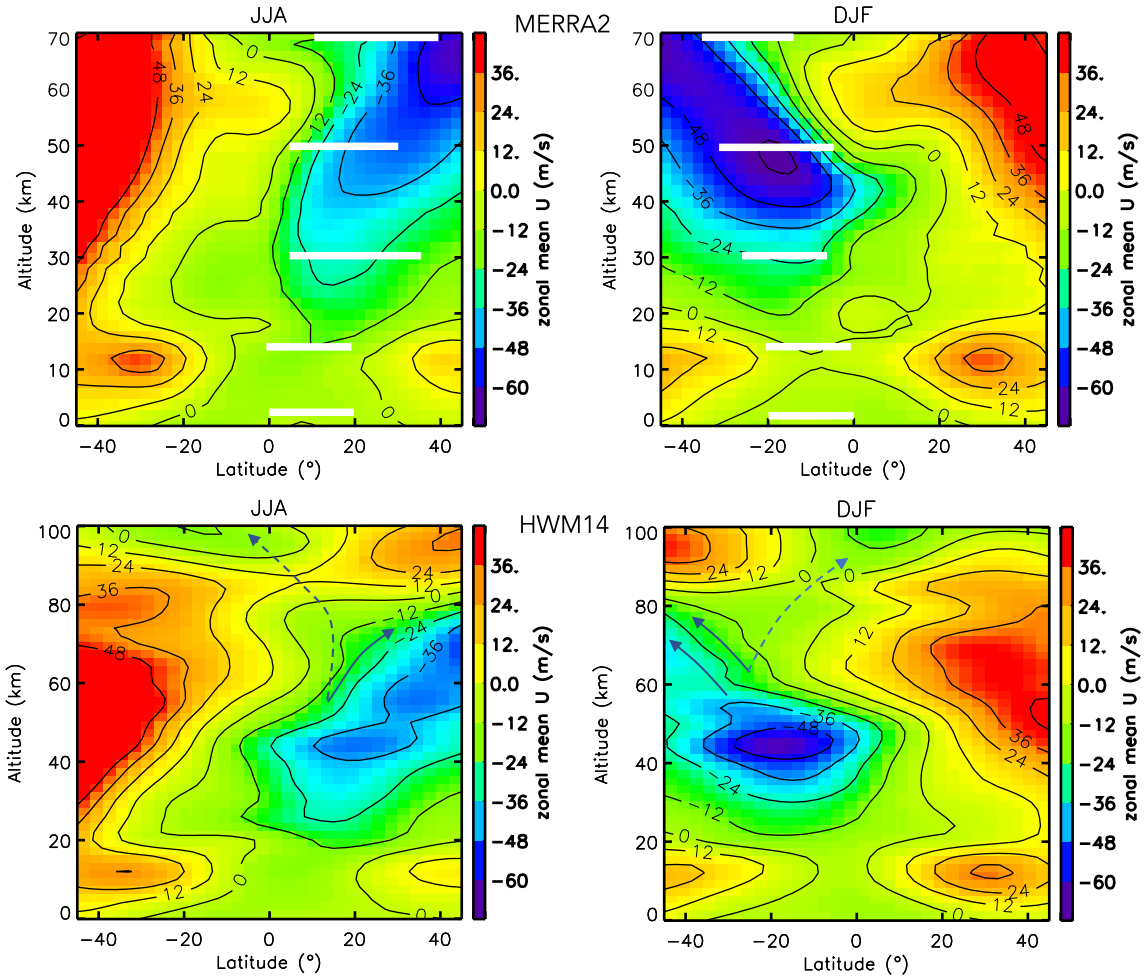

Figure 2. Height versus latitude depictions of zonal-mean zonal winds averaged over JJA (left) and DJF (right) from MERRA2 (top) extending from 0 to 70 km altitude, and from the climatological Horizontal Wind Model 2014 (HWM14, Drob et al., 2015) (bottom) extending from 0 to 100 km altitude. In the MERRA2 plots, the horizontal white bars represent the latitudinal extents of the boxes illustrated in Figure 1, which also provide a sense of the propagation channel followed by the bulk of the GWs. In the HWM14 plots, the arrows indicate alternative pathways for GWs emerging from the 60–70 km region in the SH. The pathway indicated by the dashed arrow is open depending on whether the zonal-mean winds are sufficiently negative.

Figures 1a and 1c). To complement the GW source regions alluded to in Section 3, the responses are determined by the mean GWMF values within the boxes at 30, 50, and 70 km as defined in Figures 1c–1e, respectively.

The propagation environment is defined in terms of monthly mean zonal-mean zonal winds from MERRA2 (Modern-Era Retrospective analysis for Research and Applications, Version 2) at 15, 30, 50, and 70 km. To serve as a later reference and guide for discussion, the JJA-mean and DJF-mean MERRA2 zonal winds averaged over 2016–2020 are shown in Figure 2 as a function of height (0–70 km) and latitude (45°S to 45°N). The latitudinal extents of the boxes illustrated in Figure 1 are denoted in Figure 2 with white lines, which also provide a sense of the propagation channel followed by the bulk of the GWs. Figure 2 also contains similar depictions from the climatological Horizontal Wind Model 2014 (HWM14, Drob et al., 2015), which will be used in connection with discussion of the GWMF results at 90 km. As shown below, intermonthly and interannual variability of $\overline{U}$ with respect to Figure 2 climatological means are large enough to enable quantification of wind filtering and Doppler-shift effects on the GWMFs.

As detailed by Preusse et al. (2004) in the context of GW variances in Cryogenic Limb Array Etalon Spectrometer (CLAES) temperature measurements on the Upper Atmosphere Research Satellite (UARS), there are both wind filtering and local Doppler-shifting effects to be considered in evaluating GW distributions above the troposphere, as well as instrumental limitations. Their study showed that temperature variances at 45 km altitude

were better correlated with zonal-mean zonal winds $\overline{U}$ at 25 km than those at 45 km, suggesting the importance of wind filtering at lower heights. On the other hand, in the context of GWs originating over SAm, Forbes et al. (2021) demonstrated a strong connection between GW variances at the stratopause (~50 km) and local zonal-mean winds, indicating that Doppler-shifting by the westward jet was a controlling factor. This prompted us to consider both effects in the following analysis of SABER GWMFs within the GMCS. A comparative analysis between the Forbes et al. (2021) AIM/CIPS GW variances and those derived from the TIMED/SABER measurements for SAm is also presented to provide further insight into how the "observational filter" constraints of the two instruments relate to interpretation of wind effects.

Figure 3 illustrates the outcomes of our analysis. Each colored dot represents a monthly mean value averaged over the areas displayed in Figure 1 (SAf (black), NAf (green), SAP (orange), MAP (dark blue), CAm (red), SAm (light blue)), and the accompanying standard deviations (at 1/10th their true size to enable readability) represent the variability in GWMF values over those areas. The six steps in our analysis are illustrated in Figures 3a–3f in the form of scatter plots and linear fits for the 30-km GWMF data, and a subset is provided in Figures 3g–3i for 50 km and in Figures 3j–3l for 70 km. Figures 3a–3f show, respectively: GWMF versus OLR showing a very small correlation (correlation coefficient $R = -0.10$); GWMF versus $\overline{U}$ at the GWMF observation altitude, zmU ($R = -0.70$); GWMF versus $\overline{U}$ at 15 km, zmU15 ($R = -0.50$); GWMF versus 2-parameter linear fit $\mathrm{GWMF}_{fit} = c + a \times \mathrm{OLR} + b \times \mathrm{zmU}$ ($R = 0.71$); GWMF versus 2-parameter linear fit $\mathrm{GWMF}_{fit} = c + a \times \mathrm{OLR} + b \times \mathrm{zmU15}$ ($R = 0.63$); GWMF versus 3-parameter linear fit $\mathrm{GWMF}_{fit} = c + a \times \mathrm{OLR} + b \times \mathrm{zmU} + d \times \mathrm{zmU15}$ ($R = 0.85$). For these results and all forthcoming at 50 and 70 km, no significant differences were obtained when zmU15 was replaced by zmU12 or zmU25, except for GWMF at 30 km when zmU25 is used. This exception exists because zmU25 is somewhat correlated with zmU30 ($R = 0.44$). On the other hand, zmU15 and zmU30 are not well correlated ($R = 0.19$). Additionally, insignificant differences were obtained when $\overline{U}$ is replaced with the zonal wind averaged over the local latitude × longitude area corresponding to GWMF; therefore, $\overline{U}$ and the reference altitude of 15 km for assessing wind filtering effects are used throughout.

Although there is obvious spatial correlation between enhanced regions of OLR and GWMF (see Figure 1), the result in Figure 3a suggests that little of the temporal variability in GWMF is correlated with OLR. On the other hand, an appreciable amount of GWMF variability is associated with the local zmU (Figures 3b and 3d) and to some extent zmU15 (Figures 3c and 3e), indicating that local Doppler-shifting and wind filtering at lower altitudes, respectively, are influencing the measured GWMF at 30 km. It is interesting to note that OLR variability does exert some influence when combined with zmu15 in a 2-parameter linear fit, increasing the correlation coefficient from $R = -0.50$ to $R = 0.63$; that is, compare Figures 3c and 3e. (The reader is reminded that a negative correlation between GWMF and OLR is expected on physical grounds. Lower values of OLR identify with colder cloud top temperatures, stronger convection, and presumably stronger GWs and GWMF values.) Taking R^2 as a measure of the variance captured by the fit, these correlations translate to an increase from 25% to 40% of the variance captured by the fit. Finally, combining OLR, zmU15, and zmU30 together in a 3-parameter fit, 72% of the variance ($R = 0.85$) can be captured (see Figure 3f).

Deeper insights can be gained through further examination of Figures 3b and 3c, and Figure 2. Following the propagation channels formed by the upward progression of white lines in Figure 2, below 30 km the range of mean winds encountered by GWs propagating upward from the source region between ±20° latitude is ~−35 ms^{-1} to +8 ms^{-1} (see also x-axes of Figures 3b and 3c). These values correspond roughly to the ground phase speeds (c_g) of GWs that encounter critical levels below 30 km, and are therefore absent from the GWMF spectra at 30 km and above. Accordingly, the GWMF in the summer hemisphere should be dominated by GWs of eastward (i.e., positive) ground-based phase speeds. (Actually, GWMF will be reduced in a somewhat larger spectral range around the gap caused by critical level filtering; if the intrinsic phase speed $\left(c_i = c_g - \overline{U}\right)$ of a GW becomes low yet escapes the critical level, it is nevertheless subject to dissipation due to its reduced saturation amplitude). Figure 3b also reveals a seasonal-latitudinal asymmetry imposed by the wind filtering effect. During JJA in the NH (i.e., the green, orange, and red dots corresponding, respectively, to NAf, SAP, and Cam), GWMF amplitudes benefit from the favorable propagation conditions for eastward-propagating GWs (EGWs) formed by the prevailing westward winds throughout the vertical column. On the other hand, accessibility of EGWs to 30 km during DJF in the SH (i.e., light, dark blue, and black dots corresponding, respectively, to SAm, MAP, SAf) is partially

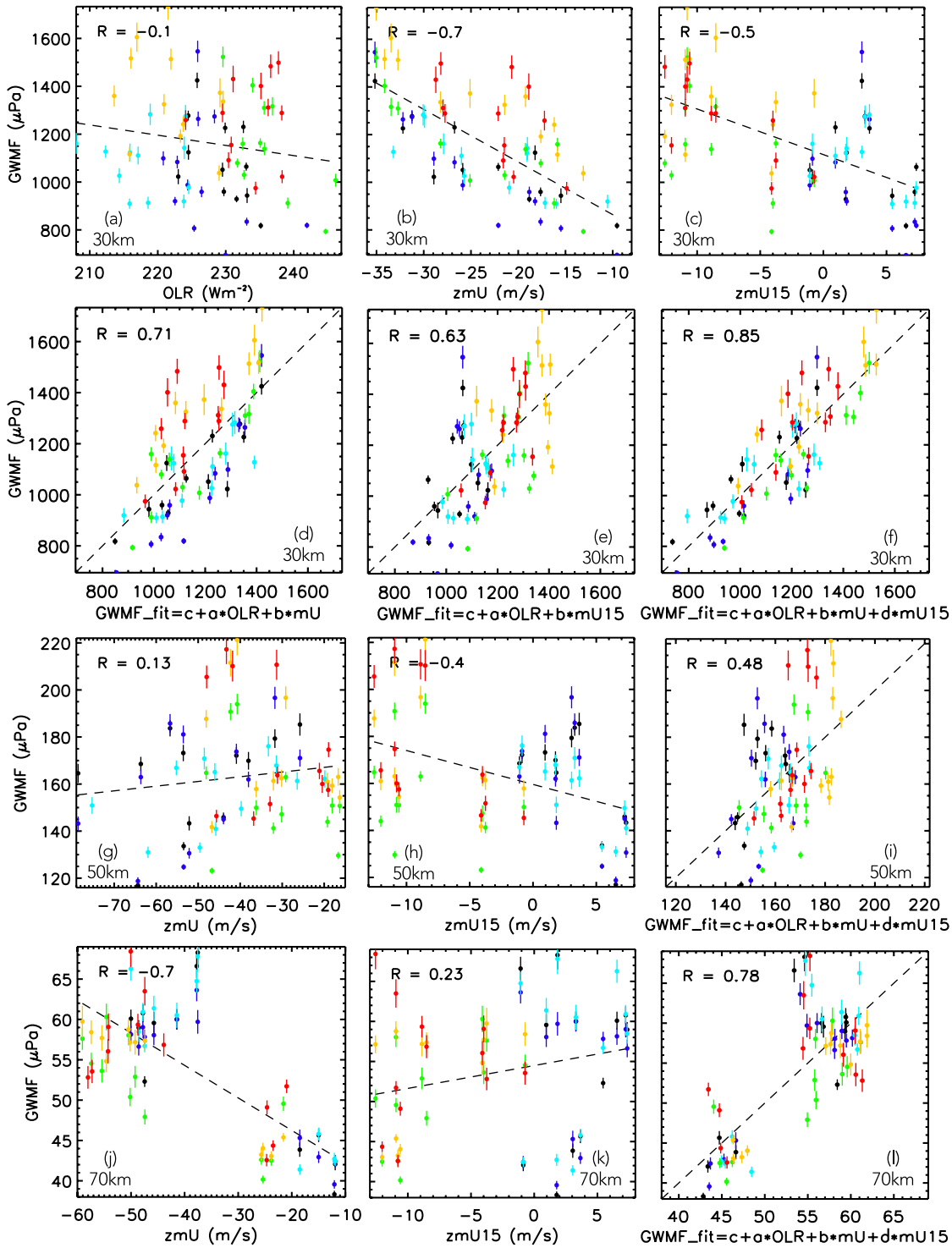

Figure 3. Scatter plots and correlation coefficients pertaining to GWMF variability relative to OLR and $\overline{U}$. Each dot represents a monthly mean value averaged over the areas displayed in Figure 1, the dashed lines represent linear fits, and standard deviations accompanying the dots (at 1/10th their true size to enable readability) represent the variability in GWMF values over those areas. The colors represent SAf (black), NAf (green), SAP (orange), MAP (dark blue), CAm (red), SAm (light blue). (a) GWMF versus OLR at 30 km. (b) GWMF versus $\overline{U}$ at 30 km, zmU. (c) GWMF versus $\overline{U}$ at 15 km, zmU15. (d) GWMF versus 2-parameter (OLR, zmU) fit values at 30 km. (e) GWMF versus 2-parameter (OLR, zmU15) fit values at 30 km. (f) GWMF versus 3-parameter (OLR, zmU, zmU15) fit values at 30 km. (g–i) same as (d–f), except at 50 km. (j–l) same as (d–f), except at 70 km.

impeded by the 0 to +8 ms^{-1} winds at 15 km, leading to lower GWMF. The deficit of DJF with respect to JJA is about 250 μPa, which is also apparent in Figures 3b and 3d.

Further analysis of the correlation in Figure 3b in terms of Doppler-shifting requires consideration of the GW viewing limitations of the SABER instrument and the connection between Doppler-shifting and GW saturation. For this purpose, the following simplified GW dispersion relation can be used to relate the c_i of a GW to its vertical wavelength λ_z (see, e.g., Preusse et al., 2004):

$$\lambda_z = \frac{2\pi}{N}|c_g - \overline{U}| = \frac{2\pi}{N}c_i \tag{1}$$

where N is the Brunt-Vaisala frequency. This is the so-called "midfrequency" approximation, which is valid for $N \gg \omega = 2\pi/\tau \gg f$ (the Coriolis parameter) τ is the intrinsic wave period, and neglects the $1/4H^2$ compressibility term relevant for $\lambda_z \gtrsim 30$ km (Fritts & Alexander, 2003). The 4–25 km λ_z and $\lambda_H \gtrsim$ 100–200 km bounds on the SABER GWMF retrievals, along with the 0.5 hr $< \tau <$ 3.5 hr bounds given below, justify use of Equation 1.

Equation 1 indicates that a GW shifted to greater c_i increases its λ_z, with obvious implications with respect to instrument observability within a certain range of λ_z. The following relations (Preusse et al., 2006; Eckerman and Preusse, 1999) will also be important for interpretations later in this paper:

$$\hat{T}_{sat} = \frac{\overline{T}}{g}N^2\frac{\lambda_z}{2\pi}, \qquad GWMF_{sat} \sim \frac{\lambda_z}{\lambda_H}\hat{T}_{sat}^2 \sim \lambda_z^3 \tag{2}$$

where $\hat{T}_{sat}$ is the saturation temperature amplitude of a GW, $GWMF_{sat}$ is the GWMF of a saturated wave, $\overline{T}$ is the background temperature, and g is the acceleration due to gravity. The important points are that a wave Doppler-shifted to a longer λ_z possesses a proportionally larger saturation amplitude, and a larger saturation $GWMF_{sat}$ that varies with cubic dependence on λ_z.

As summarized by Forbes et al. (2021, their Figure 2), GWs generated by plume overshoot (e.g., Vadas & Liu, 2009) tend to have periods <30 min and short horizontal wavelengths ($\lambda_H <$ 100–200 km), whereas those associated with mesoscale convective systems (e.g., Lane & Moncrieff, 2008, 2010; Lane & Zhang, 2011) have periods $\gtrsim$1 hr and $\lambda_H >$ 100 km. As evidenced below, the latter corresponds to the range capable of being measured by SABER. In fact, these authors present GWMF and GW momentum transport (GWMT) spectra at 20 km altitude from their "cloud system-resolving model (CSRM)" that are relevant to interpretation of results in Figure 3. Their illustrated horizontal wavenumber spectra are flat, the frequency spectra are broad with a peak near τ = 1 hr and shallow slopes toward low frequencies with only a ∼30% decrease by τ = 10 hr. The range of c_g that encompasses their results (with peaks occurring near 5, 10, or 13 ms^{-1}) is of order 5–20 ms^{-1}, which translates to $\lambda_H = c_g\tau$ = 18–720 km for τ = 1–10 hr. Applying Equation 1 with a tropical stratospheric value of N = 0.024 s^{-1} (Vincent & Alexander, 2020), this implies stratospheric λ_z in the range of 1.3–5.2 km. Applying Equation 1 to this range of c_g with $\overline{U}$ = −10 to −35 ms^{-1} (refer to x-axis of Figure 3b), the range of λ_z is Doppler-shifted to 3.9–14.4 km, which corresponds to c_i = 15–55 ms^{-1} (assuming that only eastward propagating GWs are relevant) and to $\lambda_H = c_i\tau$ = 54–1,980 km for τ = 1–10 hr. Thus, the effect of Doppler-shifting is to move a spectrum that is mostly outside the viewing sensitivity of SABER to one that is mostly within the range of observability. This appears to explain, at least in part, the increase in GWMF with respect to more westward $\overline{U}$ in Figure 3b.

However, there is a more physical explanation that may be a contributing factor at 30 km, and the necessity to invoke it arises more in connection with interpreting the contrasting weak relationship between GWMF and $\overline{U}$ relationship at 50 km altitude, which is presented further below. The physical explanation is the potential modulation of GW saturation amplitudes by Doppler-shifting. In the lower stratosphere, there is usually a portion of the GW vertical wavenumber spectrum that is saturated, resulting in a m^{-3} drop-off of the vertical wavenumber (m) spectrum at high m (see, e.g., Fritts & Alexander, 2003, and references therein), or $m > m^*$ where m^* is a characteristic wavenumber $m^* = 2\pi/\lambda_z^*$. Roughly, λ_z^* increases from about 2 km at the tropopause to 20 km at the mesopause. The general increase of λ_z^* with altitude comes from the fact that with increasing altitude the spectrum is more and more saturated, due to the general increase of GW amplitudes with altitude that accompanies decreasing density. Now consider the consequences of Doppler-shifting the GW spectrum to longer λ_z, as in our case for the eastward propagating GWs (EGWs). Saturation amplitudes increase (Equation 2), the spectrum becomes less

saturated, and less GW dissipation takes place. This implies that the higher the intrinsic phase speed of the GWs, that is, the stronger the Doppler shift, the more the GWMF can survive. Assuming a relatively saturated spectrum entering the stratosphere, the more the background wind strengthens while GWs propagate upward until reaching 30 km, the more the GW λ_z and saturation amplitudes will rise due to Doppler shift (Equation 2), and the more of the initial total source GWMF can survive. This would contribute to the positive correlation seen at 30 km in Figure 3b between GWMF and $\overline{U}$ in different months.

Figures 3g–3i provide similar depictions as in Figures 3b, 3c and 3f, except at 50 km. The correlation with OLR is similarly negligible ($R = -0.10$), and not shown. The wind filtering effect in Figure 3h is very similar to that at 30 km (Figure 3c). However, the negative correlation between GWMF and $\overline{U}$ seen at 30 km in Figure 3b is now lost at 50 km, as seen in Figure 3g. Applying the same analysis performed at 30 km and using a stratopause value of $N = 0.018$, the 5–20 ms^{-1} range of c_g and $\overline{U}$ range of −20 to −80 ms^{-1} (see x-axis of Figure 3g) translates to c_i = 25–100 ms^{-1}. The λ_z of 1.3–5.2 km are now Doppler-shifted to a range of 8.7–35.0 km, and thus a fraction of the Doppler-shifted spectrum (λ_z 25–35 km) is not visible to SABER. However, it seems unlikely that this is sufficient to account for a complete loss of correlation. Alternatively, consider that the background winds at 50 km may be sufficiently elevated compared to 30 km that the EGW spectrum at 50 km is now more widely dominated by unsaturated GWs due to the very strong Doppler shift. Our speculation is that saturation amplitudes are much higher than the amplitudes of the GWs dominating the spectrum, and therefore the differing background winds in Figure 3g do not have much effect on their momentum fluxes anymore. What still remains though is some sensitivity to the wind filtering at 15 km, as this determines which waves in the unsaturated part of the spectrum are still there.

There are also other notable differences between the 30 and 50 km results in Figures 3b and 3g, respectively. The GWMF at 50 km for both DJF and JJA are not as evenly spread with respect to $\overline{U}$ as at 30 km. In particular, note the virtual absence of JJA data (green, orange and red dots) for $\overline{U} < -50$ ms^{-1} in Figure 3g, and the sparsity of DJF data (dark/light blue, black dots) for $\overline{U} < -60$ ms^{-1}. It is possible that the GW c_g that are most affected by strong westward winds at the core of the jet differ substantially between JJA and DJF, and that the influence of the DJF 0–8 ms^{-1} c_g that are removed from the spectrum are playing a role. All of the above factors are potentially precluding a clear delineation of the Doppler-shifting effect at 50 km.

At this point, the above factors bring to mind an implicit assumption that underlies the realization of a robust correlation between GWMF and the Doppler-shift effect vis-a-vis lengthening of λ_z. In Equation 1 relating λ_z, c_g and $\overline{U}$ for a given N, any member of the c_g array of values can pair with any member of the $\overline{U}$ array to result in a lengthening of λ_z and potential modification of GWMF amplitude. A robust correlation is much more likely to occur if GWMF amplitudes are constant across the range of c_g = 5–20 ms^{-1}, and/or if the GWMF are concentrated near a single c_g. However, such conditions are likely to exist to varying degrees, and undoubtedly represent a contributing factor to the scatter and limited correlations in all of the panels of Figure 3, and perhaps in extreme cases the absence of any significant correlation, as in Figure 3g. It is noteworthy, though, that examples of GWMF or GWMT spectra at 20 km shown in Lane and Moncrieff (2008, 2010) and Lane and Zhang (2011) maximize near c_g of ±5, 10, or 13 ms^{-1}, but it is not known to what extent these examples are representative of the broad range of conditions considered here.

The same sequence of three scatter plots is shown for 70 km in Figures 3j, 3k and 3l. In Figure 3j, the weak westward $\overline{U}$ correspond to February and August, and the stronger westward $\overline{U}$ correspond to the remaining months, leaving a gap in the middle that is unrelated to GWMF per se. Note that with elimination of the westward winds with amplitudes greater than 60 ms^{-1} that are present at 50 km (i.e., Figure 3g), the signature of a Doppler-shifting effect has returned with correlation coefficient $R = -0.7$ between GWMF and $\overline{U}$. Assuming a mesospheric value of $N = 0.018$/s, and $\overline{U}$ −10 to −60 ms^{-1} applied to the same c_g range of 5–20 ms^{-1}, we arrive at a λ_z range of 9.8–28.0 km, that also takes into account (at the lower end) a minimum λ_H of 100 km. This λ_z range nearly falls within the 4–25 km range observable by SABER. So it seems that the part of the GW spectrum that was removed from SABER observability at 50 km is now returned at 70 km, and this may account for some improvement in the correlation between GWMF and $\overline{U}$. But again, since this apparently does not involve a major portion of the spectrum, there must be more to the story. To the point, between 50 and 70 km the GW spectrum becomes more saturated due to the general amplitude growth accompanying the density decrease with altitude. Moreover, the resulting GW drag reduces the background winds and even strengthens the saturation effect because the spectrum

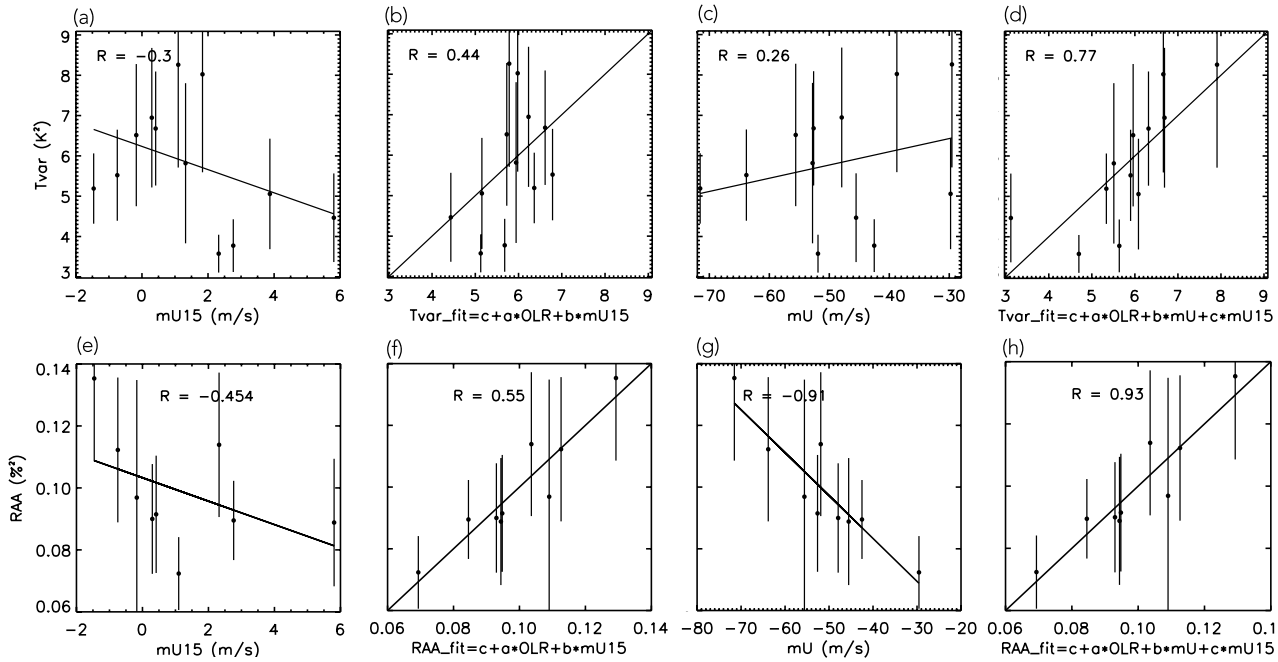

Figure 4. Similar to Figure 3, except for GWs at 50 km associated with South American continental convective sources during DJF. Top: Temperature variances from SABER. Bottom: RAA_v from CIPS.

is shifted to higher m again (the Doppler shift is reduced). As parts of the GW spectrum are now saturated again, this reintroduces the sensitivity to $\overline{U}$ seen in Figure 3j.

4.2. SABER-CIPS Comparison at 50 km

Since the Forbes et al. (2021) study was a motivating influence for conducting the present study, a comparison between the GW response at 50 km to GWs originating over SAm from CIPS and SABER is now presented. CIPS is a nadir-looking imager sensitive to GWs with $\lambda_z > 15$ km and λ_H between about 23 and 600 km. Both studies define a similar SAm source region confined to the mainland of SAm between 0° and 20°S. However, the CIPS study used RR to define source variability, and examined Rayleigh Albedo Anomaly variance (RAA_v), which is closely related to temperature variance, to represent the GW response over a similar latitude × longitude region as SABER at 50 km. To achieve a greater degree of consistency, the present study was redone using temperature variance (T_v), and the CIPS study was redone using OLR as a proxy for GW source variability. However, the SABER results for SAm were performed for all 12 DJF months from 2016 to 2020, whereas the three DJF months for SH 2017–2018 summer were omitted for CIPS due to background noise as described in Forbes et al. (2021).

The SABER-CIPS comparison is presented in Figure 4, and consists of the same types of panels as in Figure 3. This comparison also provides the opportunity to display typical standard deviations associated with the latitude × longitude area means, which were reduced in size to provide acceptable readability of the 72 colored points in each panel of Figure 3. Figure 4a illustrates a negative ($R = -0.3$) correlation with $\overline{U}$ at 15 km, and when combined with OLR in a 2-parameter fit yields an $R = +0.44$ (Figure 4b). The plot of T_v with respect to $\overline{U}$ at 50 km in Figure 4c yields a small positive correlation ($R = +0.26$) similar to that of the whole GMCS depicted in Figure 3g ($R = +0.13$), where the light blue dots represent SAm. The same speculations made there to explain the absence of a robust correlation related to Doppler-shifting apply here. Finally, the 3-parameter fit in Figure 4d yields $R = +0.77$, significantly better than the $R = +0.48$ for the whole GMCS in Figure 3i. With respect to SABER T_v, OLR, $\overline{U}$ at 15 km, and $\overline{U}$ at 50 km all reflect modest correlations individually, but when combined together in a 3-parameter fit capture 59% of the variance.

The same sequence of information is provided in Figures 4e–4h for CIPS RAA_v. Figure 4e shows a $R = -0.45$ correlation between RAA_v and $\overline{U}$ at 15 km, reflecting a similar wind-filtering effect as SABER T_v. When combined

with OLR in a 2-parameter fit, a $R = +0.55$ is achieved, slightly better than the $R = +0.44$ for T_v (Figure 4b). However, in contrast to the small positive correlation ($R = +0.26$, Figure 4c) between T_v and $\overline{U}$ for SABER, a remarkably high ($R = -0.91$) correlation exists between RAA_v and $\overline{U}$ at 50 km (Figure 4g), leading to $R = +0.93$ in a 3-parameter fit with 86% of the variance now captured.

The primary result to emerge from Figure 4 is that RAA_v reflects a robust negative correlation with $\overline{U}$ at 50 km, whereas SABER T_v exhibits a weak positive correlation, all other aspects being approximately the same. Noting that CIPS is only sensitive to $\lambda_z > 15$ km, the RAA_v with λ_z of 1.3–5.2 km and associated with the assumed source spectrum of $c_g = 5$–20 ms^{-1} is invisible to CIPS for $\overline{U} = 0$, but becomes increasingly visible to the CIPS instrument as $\overline{U}$ becomes increasingly negative. On the other hand, it was deduced in the discussion pertaining to Figures 3a–3i that the low SABER correlation at 50 km is due to the low degree of saturation of the spectrum of eastward GWs (EGWs). For SABER, observational filter effects are there, but probably less important, as the main part of the EGW spectrum should be still visible. This appears to be the crux of the argument explaining the difference between results in Figures 4c and 4g. The apparent reappearance of some waves when $\overline{U}$ becomes less negative at 70 km (cf., Figure 3j) is also consistent with this argument. A more refined analysis requires knowledge of the true nature and variability of the c_g spectra, and whether the part of the spectrum with λ_H between 23 km and 100–200 km seen by CIPS and not SABER is also playing a role.

5. GWMF Variability at 90 km

Figure 5 presents latitude versus longitude plots of SABER GWMF at 90 km for January and July 2017–2020. All of the 90-km results exhibit considerable intraseasonal and interannual variability, and these months are chosen as typical examples, and because they represent the height of convective activity in both hemispheres. January 2018 is notable due to the 4 maxima near the equator that occur about 30° eastward and 10° equatorward of the OLR maxima designated SAf, MAP, and SAm in Figure 1a. A similar series of maxima, displaced somewhat from those in January 2018, occurs during January 2019. Interestingly, a series of similarly spaced four maxima appear in the vicinity of 40°N during January 2020, and during January 2017 there are no ordered distributions of maxima to be found. In Supporting Information S1, the reader will find that during December and February months there exists a variety of structures, ranging from two to four clear maxima to a nearly featureless distribution (e.g., February 2017).

Similar features can be found in the July GWMF distributions at 90 km in Figure 5. July 2020 is characterized by 3 near-equatorial maxima that appear connected to more intense ones near 40°N. Somewhat less ordered versions of the same types of connections exist for July 2017, 2018, and 2019, and in some cases connections between the equatorial maxima and those in SH mid latitudes exist, and these types of features can also be seen in some other months in Supporting Information S1.

The net result of this brief summary is that at 90 km there appear to be vestiges of the GWMF structures that exist at low latitudes, but their locations at 90 km are not as stable and predictable, and in fact may not even be confined to the same hemisphere as those at lower altitudes. And, at this point we get the sense that the AR distribution at 90 km in Figure 1f may bear some consistency with the summary just provided. Since the $\overline{U}$ distributions have guided our interpretations so far, we now seek to examine what insights can be provided by the HWM14 mean winds depicted in Figure 2. It is noted that HWM14 captures the salient features of MERRA2 below 70 km. This combined with the knowledge that HWM14 winds above 80 (100) km are rooted in wind measurements from ground-based radars (satellite-based instruments) over the globe, provides confidence that HWM14 can provide some useful insights into the interpretation of SABER GWMF measurements at 90 km.

Starting with both DJF and JJA in the summer hemispheres, it is evident from the HWM14 panels in the lower half of Figure 2 that there is a reversal at about 80 km from westward winds below to eastward winds above between about 10° and 45°N. It is well established, for example, Holton (1983), Miyoshi et al. (2014), and Schmidt et al. (2006) that the latter result from dissipation and deposition of eastward momentum associated with the EGWs discussed throughout this paper. But there are alternative pathways for these EGWs, for example, following along the -12 ms^{-1} contours of the easterly jet to middle and perhaps higher latitudes in the vicinity of 80 km in both hemispheres, as indicated by the solid arrows. In fact, we note from the Thurairajah et al. (2017) analysis of SABER GWMF during NH summer 2007 that the maximum GWMF occurs near 80 km altitude and

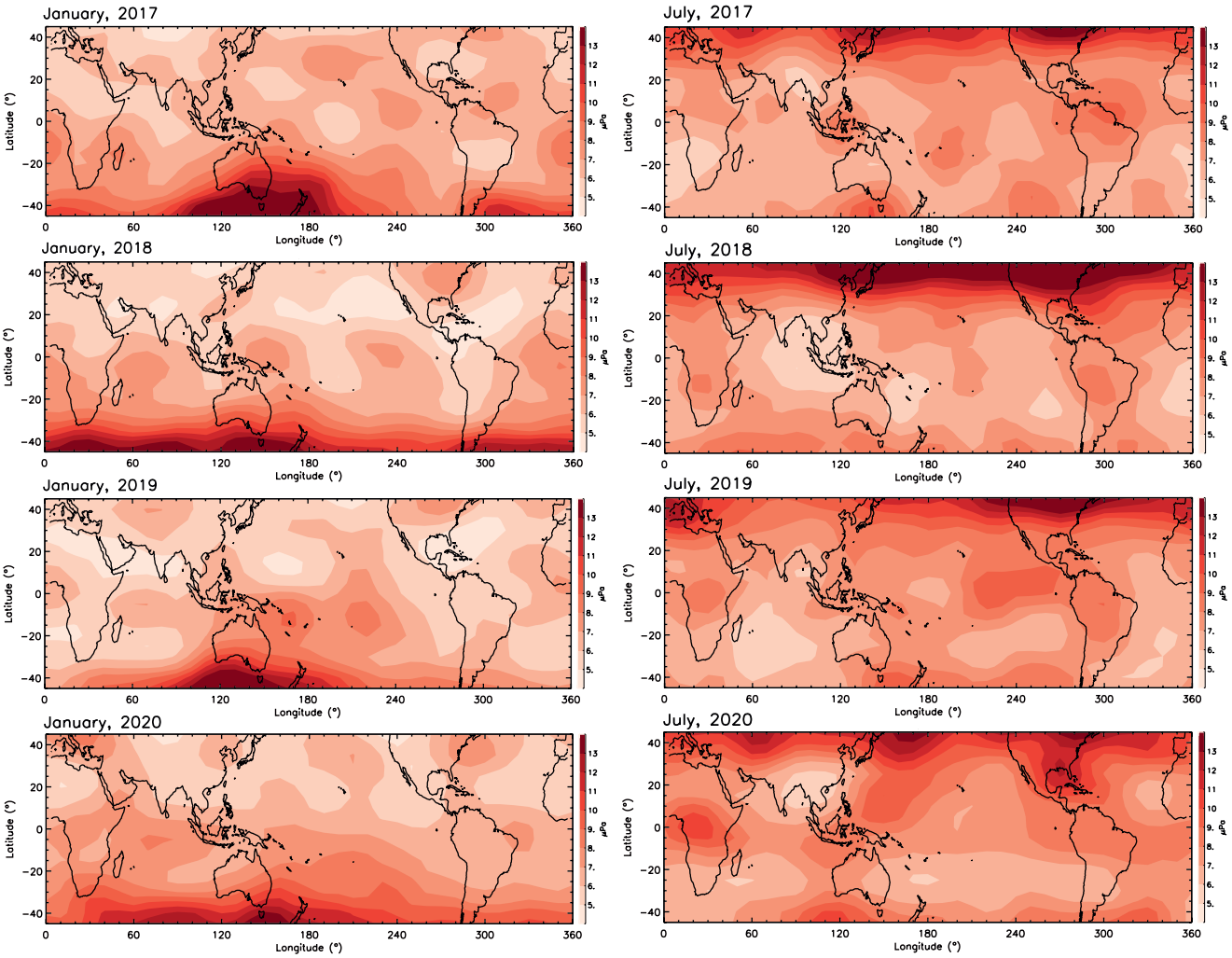

Figure 5. Typical examples of SABER GWMF distributions at 90 km. Left (Right): January (July) for 2017, 2018, 2019, 2020 (top to bottom).

45°N, coincident with the intersection of the −12 ms^{-1} contour and 45°N during JJA in Figure 2. During DJF there is also a pathway extending from the jet core to the equator near 90–100 km, along the weak westward winds between the 0 ms^{-1} contours, as indicated by the dashed arrow. Such a propagation path toward the equator and low southern latitudes also exists during JJA, but as drawn is only open to the higher-phase speed (>12 ms^{-1}) EGW. A likely scenario is that all of the propagation paths just discussed are subject to considerable variability from month to month, and that the varieties of multipeaked structures in Figure 5 and Supporting Information S1 reflect the different degrees of accessibility to higher altitudes and/or higher latitudes that these variable propagation paths offer.

In the vicinity of 90 km, solar tides serve as a likely source for Doppler-shifting GWs in a way that influences the propagation paths noted above. The ascending and descending orbital segments of the TIMED satellite that carries the SABER instrument each take 120 days to precess through 24 hr of local time. Over shorter time periods, nonmigrating (solar asynchronous) tides manifest as wave-k longitude variations where $k = |s - n|$, n denotes the wave frequency (day^{-1}), and s is the zonal wavenumber of the tide. Two of the largest nonmigrating tides are the eastward-propagating diurnal ($n = 1$) tides with zonal wavenumbers $s = -2$ (DE2) and $s = -3$ (DE3) (e.g., Truskowski et al., 2014). Therefore, DE2 (DE3) presents a $k = 3$ ($k = 4$) longitude variation. The first symmetric components of these tidal components are actually diurnal Kelvin waves characterized by zonal winds broadly distributed about the equator with a Gaussian shape. So the suggestion is that nonmigrating tides maybe be modifying propagation paths at 90 km in a way that also imposes latitude × longitude variability of

the type illustrated in Figure 5. In addition, the tides could introduce wind variations that lead to dissipation of parts of the GW spectrum. Empirical evidence that tidal influences exist can be found in the recent work of Ern et al. (2021). In that paper, it is shown that GW-drag-proxy maxima at ± 10° latitudes above ~80 km altitude are phase-shifted by ~180° between ascending and descending SABER orbit data (see Figure 8 in this paper). These maxima shift upward with time, in agreement with the local time shift during TIMED/SABER orbit precession, a likely signature of phase-locking with tides.

6. Summary and Conclusions

1. Organization of the Global Monsoon System (GMS) in terms of annual range (AR = |DJF − JJA|/(DJF − JJA)) and convective intensity using OLR as a proxy leads to definition of the Global Monsoon *Convective* System (GMCS) consisting of 6 tropical regions: North and South Africa (NAf, SAf), Central and South America (CAm, SAm), and the South Asia-Pacific and Malay Archipelago/Australia-Pacific regions (SAP, MAP). About half the geographic areas of SAP and MAP are oceanic. Definition of the GMCS in this fashion leads to much tighter and more well-defined geographic regions than is the case when the GMS is defined according to AR in rainfall rate.
2. Annual ranges of GWMF determined from TIMED/SABER measurements at 30, 50, and 70 km altitude are also organized into six tropical regions that can be connected on a one-to-one basis with those defined with respect to OLR, suggesting source-response relationships.
3. The GWMF longitudinal structures in each hemisphere (comprising 3 maxima) shift increasingly poleward with altitude, linked to the favorable propagation conditions formed by the upward/poleward tilt of the summer easterly jets.
4. For each geographic region at each altitude, monthly mean values of OLR and monthly mean values of GWMF are defined for the DJF and JJA months between December 2016 and August 2020. This leads to 72 OLR-GWMF pairs (six regions × 12 months) at each altitude that can be used to obtain the source-response relationships that define the *extended* GMCS as a whole.
5. The effects of mean winds on the source-response relationships are introduced in terms of multiple linear regression fits that express GWMF in terms of OLR, MERRA2 zonal-mean winds $\left(\overline{U}\right)$ at 15 km latitude, and MERRA2 $\overline{U}$ at the individual heights of 30, 50, and 70 km. Based on visual examination of the MERRA2 $\overline{U}$ contours intersecting the white bars in Figure 2, as well as for individual months (not shown), the winds at 12–15 km altitude are assumed to represent the bulk of wind filtering effects on the vertically propagating EGWs that reside within the summer easterly jet. In other words, filtering by winds at altitudes above 15 km are of secondary importance, at least for this special situation. However, this assumption may not be more broadly applicable to other situations. The winds at the individual heights of 30, 50, and 70 km can reveal (a) the presence of Doppler-shift effects, which includes the introduction of different degrees of GW saturation that influence the correlation with local winds and (b) modification of vertical wavelengths in a way that can move the GWs into or out of the λ_z = 4–25 km limitations of the SABER GW retrieval.
6. To pursue a deeper understanding of the linear regression fits, a source spectrum had to be defined. Based on numerical simulations of mesoscale convective systems, a range of ground-based phase speeds c_g = 5–20 ms^{-1} (eastward) at 20 km altitude was assumed. Based on the midfrequency GW dispersion relation approximation, this implies a range of vertical wavelengths λ_z of 1.3–5.2 km. This range of c_g is assumed constant for all 12 months and both hemispheres. Note that this spectrum excludes high-phase-speed GWs generated by plume overshoot, which generally have longer λ_z and shorter λ_H than can be seen by SABER.
7. At 30 km, OLR, wind filtering, and Doppler-shifting are all found to play roles in achieving a correlation coefficient between the fit and measured GWMFs of R = +0.85, implying that 72% (R^2) of the variance is captured. It appears that Doppler-shifting effects on instrument sensitivity and through modulation of the saturated GW spectrum may both be playing roles in explaining this high correlation.
8. At 50 km, OLR and wind filtering play roles, leading to R = +0.47 for the 2-parameter fit. However, the correlation between GWMF and $\overline{U}$, which include westward wind speeds up to −80 ms^{-1}, is only R = +0.13. This leads to a R = +0.48 for the 3-parameter fit, implying that only 23% of the GWMF variance is captured, markedly less than the 72% at 30 km. To explain this disparity, it is hypothesized that the large $\overline{U}$ result in higher saturation amplitudes due to the Doppler shift effect, leading to desaturation of a large

portion of the spectrum, and therefore lack of sensitivity of GWMFs associated with desaturated GWs to changes in $\overline{U}$. It is also estimated that the largest $\overline{U}$ push the longest λ_z parts of the spectrum to $\lambda_z > 25$ km, out of the sensitivity range of SABER; however, it appears doubtful that this is the dominant effect.

9. At 70 km, where the maximum westward $\overline{U}$ is 60 ms^{-1}, a stronger correlation ($R = -0.70$) between GWMF and local $\overline{U}$ exists, leading to a correlation with the 3-parameter fit of +0.78 (61% of variance captured). In this case, OLR, wind filtering, and instrument sensitivity play secondary roles. Our hypothesis is that between 50 and 70 km the GW spectrum becomes more saturated again due to the general amplitude growth due to density decrease with altitude. $\overline{U}$ and the Doppler shift are also reduced due to the resulting GW drag, adding to the saturation. The net effect is to reintroduce the sensitivity to $\overline{U}$ that existed at 30 km.
10. The above results at 30, 50, and 70 km are virtually the same whether $\overline{U}$ is defined as an average within individual longitude sectors, or as a zonal average; therefore, the latter was chosen for displaying all results.
11. A comparison was performed between GW variances obtained by SABER and CIPS at 50 km during DJF, and confined to the South American sector. In this case, the SABER results captured 59% of the variance ($R = +0.77$) with OLR, wind filtering, and Doppler effects all playing roles. The same is true for CIPS, but an overall correlation of $R = +0.93$ is achieved (86% of variance captured). For CIPS, the correlation between variance and local $\overline{U}$ is $R = -0.91$, in contrast to $R = +0.26$ for SABER. In the case of CIPS, this relationship is strongly influenced by parts of the spectrum being Doppler-shifted into its $\lambda_z > 15$ km viewing range, and by increased saturation amplitudes. For SABER, we deduce that the low correlation with $\overline{U}$ is likely driven by the low degree of saturation of the spectrum, and the fact that SABER observes a larger range of the unsaturated part of the GW spectrum than CIPS. The unsaturated GWs seen by SABER are less sensitive to the background wind at this altitude, but still sensitive to source variations and wind filtering near the source.
12. It is noted that there is a limit on how good any of the above correlations can be, due to variations in the amplitude of the c_g spectrum, which we have assumed to be constant throughout our analysis.
13. At 90 km, SABER GWMFs are characterized by responses spanning both hemispheres, considerable variability between months, sometimes irregularly distributed maxima, and sometimes well-organized 2-, 3-, and 4-peaked maxima with respect to longitude with connections to other latitudes. It is well established (e.g., Holton, 1983; Miyoshi et al., 2014; Schmidt et al., 2006) that the middle atmosphere jets in both hemispheres shift to oppositely directed weaker jets above about 80 km altitude. This is due to the effects of selective filtering of GWs by the jets, and by dissipation and momentum deposition of the oppositely directed GWs above ∼80 km. In the zonal-mean context, this arrangement leaves open propagation pathways between the lower and upper jets, and between the upper jets in the equatorial region, that can in principle enable GW accessibility to a wider range of latitudes including the opposite hemisphere. The dependence of these upper jets on the variable nature of the GW spectrum responsible for their formation suggests that the propagation pathways are also likely to vary from month the month and between hemispheres. In addition, at 90 km, further modification of the background wind field (and associated Doppler-shifting of λ_z) in latitude and longitude presented to GWs is possible through the presence of solar tides, in particular diurnal Kelvin waves that are characterized by broad, Gaussian-shaped zonal wind distributions about the equator. We present arguments and empirical observational evidence to the effect that solar tides can introduce latitude and longitude variability into the GW propagation environment at $\gtrsim$90 km commensurate with the types of variability seen in the SABER GWMF distributions at 90 km.
14. Another potential contributor to the spatial-temporal variability of GWMFs at 90 km is the likelihood that some waves are reaching saturation amplitudes, dissipating, and exciting secondary waves between 70 and 90 km.

Abbreviations, Acronyms, and Symbols

AIM	Aeronomy of Ice in the Mesosphere
AR	Annual Range
CAm	Central America
CIPS	Cloud Imaging and Particle Size
CLAES	Cryogenic Limb Array Etalon Spectrometer
DJF	December-January February

EGWs	eastward-propagating gravity waves
GMCS	Global Monsoon Convective System
GMS	Global Monsoon System
GPMM	Global Precipitation Measurement Mission
GW(s)	gravity wave(s)
GWMF(s)	gravity wave momentum flux(es)
HWM14	Horizontal Wind Model 2014
JJA	June-July-August
λ_H	GW horizontal wavelength
λ_z	GW vertical wavelength
MAP	Malay Archipelago/Australia-Pacific
MERRA2	Modern-Era Retrospective analysis for Research and Applications, Version 2
NH	Northern Hemisphere
NAf	North Africa
OLR	Outgoing Longwave Radiation
RAA_v	Rayleigh Albedo Anomaly Variance
RR	Rainfall Rate
SABER	Sounding of the Atmosphere using Broadband Emission Radiometry
SH	Southern Hemisphere
SAf	South Africa
SAm	South America
SAP	South Asia-Pacific
SPCZ	South Pacific Convergence Zone
TIMED	Thermosphere Ionosphere Mesosphere Energetics and Dynamics
T_v	Temperature variance
$\overline{U}$	zonal- and diurnal-mean zonal wind
UARS	Upper Atmosphere Research Satellite

Data Availability Statement

The daily OLR data were obtained from https://psl.noaa.gov/data/gridded/data.olrcdr.interp.html (Liebmann & Smith, 1996). The RR data correspond to "Level-3 Integrated Multi-satellite Retrievals for GPM (IMERG) Final Run" (Huffman et al., 2014), and were downloaded from https://gpm.nasa.gov/data/directory. This data product results from merging, intercalibrating, and interpolating all available satellite precipitation estimates and rain gauge data over the globe. MERRA2 winds were obtained from https://gmao.gsfc.nasa.gov/reanalysis/MERRA-2/ (Gelaro et al., 2017). The SABER GWMF and Tvar datasets can be found at https://doi.org/10.5281/zenodo.6343173 and https://doi.org/10.5281/zenodo.6346343, respectively (Ern et al., 2022a, 2022b).

Acknowledgments
JMF and XZ acknowledge support for this work by NASA Award 80NSSC18K0775 to the University of Colorado under the Heliophysics Guest Investigator Program. ME acknowledges support for this work by the German Federal Ministry of Education and Research (BMBF) Grant 01LG1905C (QUBICC, ROMIC).

References

Alexander, M. J. (1998). Interpretations of observed climatological patterns in stratospheric gravity wave variance. *Journal of Geophysical Research*, *103*(D8), 8627–8640. https://doi.org/10.1029/97JD03325

Alexander, M. J., Geller, M., McLandress, C., Polavarapu, S., Preusse, P., Sassi, F., et al. (2010). Recent developments in gravity wave effects in climate models, and the global distribution of gravity wave momentum flux from observations and models. *The Quarterly Journal of the Royal Meteorological Society*, *136*(650), 1103–1124. https://doi.org/10.1002/qj.637

Chen, D., Strube, C., Ern, M., Preusse, P., & Riese, M. (2019). Global analysis for periodic variations in gravity wave squared amplitudes and momentum fluxes in the middle atmosphere. *Annales Geophysicae*, *37*(4), 487–506. https://doi.org/10.5194/angeo-37-487-2019

Choi, H.-J., Chun, H.-Y., & Song, I.-S. (2009). Gravity wave temperature variance calculated using the ray-based spectral parameterization of convective gravity waves and its comparison with Microwave Limb Sounder observations. *Journal of Geophysical Research*, *114*(D8), D08111. https://doi.org/10.1029/2008JD011330

Drob, D. P., Emmert, J. T., Meriwether, J. W., Makela, J. J., Doornbos, E., Conde, M., et al. (2015). An update to the Horizontal Wind Model (HWM): The quiet time thermosphere. *Earth and Space Science*, *2*(7), 301–319. https://doi.org/10.1002/2014EA000089

Eckermann, S. D., & Preusse, P. (1999). Global measurements of stratospheric mountain waves from space. *Science*, *286*, 1534–1537. https://doi.org/10.1126/science.286.5444.1534

Ern, M., Diallo, M., Preusse, P., Mlynczak, M. G., Schwartz, M. J., Wu, Q., & Riese, M. (2021). The semiannual oscillation (SAO) in the tropical middle atmosphere and its gravity wave driving in reanalyses and satellite observations. *Atmospheric Chemistry and Physics*, *21*(18), 13763–13795. https://doi.org/10.5194/acp-21-13763-2021

Ern, M., Forbes, J. M., & Zhang, X. (2022a). SABER gravity wave absolute momentum fluxes for the global monsoon seasons 2016–2020 [Data set]. Zenodo. https://doi.org/10.5281/zenodo.6343173

Ern, M., Forbes, J. M., & Zhang, X. (2022b). SABER gravity wave temperature variances for the global monsoon seasons 2016–2020 [Data set]. Zenodo. https://doi.org/10.5281/zenodo.6346343

Ern, M., Hoffmann, L., & Preusse, P. (2017). Directional gravity wave momentum fluxes in the stratosphere derived from high-resolution AIRS temperature data. *Geophysical Research Letters*, *44*(1), 475–485. https://doi.org/10.1002/2016GL072007

Ern, M., Preusse, P., Alexander, M. J., & Warner, C. D. (2004). Absolute values of gravity wave momentum flux derived from satellite data. *Journal of Geophysical Research*, *109*(D20), D20103. https://doi.org/10.1029/2004JD004752

Ern, M., Preusse, P., Gille, J. C., Hepplewhite, C. L., Mlynczak, M. G., Russell, J. M., III, & Riese, M. (2011). Implications for atmospheric dynamics derived from global observations of gravity wave momentum flux in stratosphere and mesosphere. *Journal of Geophysical Research*, *116*(D19), D19107. https://doi.org/10.1029/2011JD015821

Ern, M., Preusse, P., & Riese, M. (2015). Driving of the SAO by gravity waves as observed from satellite. *Annales Geophysicae*, *33*(4), 483–504. https://doi.org/10.5194/angeo-33-483-2015

Ern, M., Trinh, Q. T., Preusse, P., Gille, J. C., Mlynczak, M. G., Russell, J. M., III, & Riese, M. (2018). GRACILE: A comprehensive climatology of atmospheric gravity wave parameters based on satellite limb soundings. *Earth System Science Data*, *10*(2), 857–892. https://doi.org/10.5194/essd-10-857-2018

Fetzer, E. J., & Gille, J. C. (1994). Gravity wave variance in LIMS temperatures. Part I: Variability and comparison with background winds. *Journal of the Atmospheric Sciences*, *51*(17), 2461–2483. https://doi.org/10.1175/1520-0469(1994)051<2461:GWVILT>2.0.CO;2

Forbes, J. M., Zhang, X., Randall, C. E., France, J., Harvey, V. L., Carstens, J., & Bailey, S. M. (2021). Troposphere- mesosphere coupling by convectively forced gravity waves during Southern Hemisphere monsoon season as viewed by AIM/CIPS. *Journal of Geophysical Research: Space Physics*, *126*(11), e2021JA029734. https://doi.org/10.1029/2021JA029734

Fritts, D. C., & Alexander, M. J. (2003). Gravity wave dynamics and effects in the middle atmosphere. *Reviews of Geophysics*, *41*(1). 3-1–3-64. https://doi.org/10.1029/2001RG000106

Gelaro, R., McCarty, W., Suarez, M. J., Todling, R., Molod, A., Takacs, L., et al. (2017). The Modern-Era Retrospective analysis for Research and Applications, version 2 (MERRA-2). *Journal of Climate*, *30*(14), 5419–5454. https://doi.org/10.1175/JCLI-D-16-0758.1

Hoffmann, L., Xue, X., & Alexander, M. J. (2013). A global view of stratospheric gravity wave hotspots located with Atmospheric Infrared Sounder observations. *Journal of Geophysical Research: Atmospheres*, *118*(2), 416–434. https://doi.org/10.1029/2012jd018658

Holton, J. R. (1983). The influence of gravity wave breaking on the general circulation of the middle atmosphere. *Journal of the Atmospheric Sciences*, *40*(10), 2497–2507. https://doi.org/10.1175/1520-0469(1983)040<2497:tiogwb>2.0.co;2

Huffman, G., Bolvin, D., Braithwaite, D., Hsu, K., Joyce, R., & Xie, P. (2014). *Integrated Multi-satellitE Retrievals for GPM (IMERG), version 5.2*. NASA's Precipitation Processing Center. Retrieved from https://gpm.nasa.gov/sites/default/files/document_files/IMERG_ATBD_V5.2_0.pdf

Jia, J. Y., Preusse, P., Ern, M., Chun, H.-Y., Gille, J. C., Eckermann, S. D., & Riese, M. (2014). Sea surface temperature as a proxy for convective gravity wave excitation: A study based on global gravity wave observations in the middle atmosphere. *Annales Geophysicae*, *32*(11), 1373–1394. https://doi.org/10.5194/angeo-32-1373-2014

Jiang, J. H., Wang, B., Goya, K., Hocke, K., Eckermann, S. D., Ma, J., et al. (2004). Geographical distribution and interseasonal variability of tropical deep convection: UARS MLS observations and analyses. *Journal of Geophysical Research*, *109*(D3), D03111. https://doi.org/10.1029/2003JD003756

Kalisch, S., Preusse, P., Ern, M., Eckermann, S. D., & Riese, M. (2014). Differences in gravity wave drag between realistic oblique and assumed vertical propagation. *Journal of Geophysical Research: Atmospheres*, *119*(17), 10081–10099. https://doi.org/10.1002/2014JD021779

Lane, T. P., & Moncrieff, M. W. (2008). Stratospheric gravity waves generated by multiscale tropical convection. *Journal of the Atmospheric Sciences*, *65*(8), 2598–2614. https://doi.org/10.1175/2007JAS2601.1

Lane, T. P., & Moncrieff, M. W. (2010). Characterization of momentum transport associated with organized moist convection and gravity waves. *Journal of the Atmospheric Sciences*, *67*(10), 3208–3225. https://doi.org/10.1175/2010JAS3418.1

Lane, T. P., & Zhang, F. (2011). Coupling between gravity waves and tropical convection at mesoscales. *Journal of the Atmospheric Sciences*, *68*(11), 2582–2598. https://doi.org/10.1175/2011JAS3577.1

Liebmann, B., & Smith, C. A. (1996). Description of a complete (interpolated) outgoing longwave radiation dataset. *Bulletin of the American Meteorological Society*, *77*, 1275–1277.

Liu, H., Pedatella, N., & Hocke, K. (2017). Medium-scale gravity wave activity in the bottomside F region in tropical regions. *Geophysical Research Letters*, *44*(14), 7099–7105. https://doi.org/10.1002/2017GL073855

Liu, H.-L., McInerney, J. M., Santos, S., Lauritzen, P. H., Taylor, M. A., & Pedatella, N. M. (2014). Gravity waves simulated by high-resolution Whole Atmosphere Community Climate Model. *Geophysical Research Letters*, *41*(24), 9106–9112. https://doi.org/10.1002/2014GL062468

Liu, J., Wang, B., Ding, Q. H., Kang, X. Y., Soon, W., & Zorita, E. (2009). Centennial variations of the global monsoon precipitation in the last millennium: Results from ECHO-G model. *Journal of Climate*, *22*(9), 2356–2371. https://doi.org/10.1175/2008jcli2353.1

McLandress, C., Alexander, M. J., & Wu, D. L. (2000). Microwave Limb Sounder observations of gravity waves in the stratosphere: A climatology and interpretation. *Journal of Geophysical Research*, *105*(D9), 11947–11967. https://doi.org/10.1029/2000JD900097

Miyoshi, Y., Fujiwara, H., Jin, H., & Shinagawa, H. (2014). A global view of gravity waves in the thermosphere simulated by a general circulation model. *Journal of Geophysical Research: Space Physics*, *119*(7), 5807–5820. https://doi.org/10.1002/2014ja019848

Park, J., Lühr, H., Lee, C., Kim, Y. H., Jee, G., & Kim, J.-H. (2014). A climatology of medium-scale gravity wave activity in the midlatitude/low-latitude daytime upper thermosphere as observed by CHAMP. *Journal of Geophysical Research: Space Physics*, *119*(3), 2187–2196. https://doi.org/10.1002/2013JA019705

Preusse, P., Eckermann, S. D., Ern, M., Oberheide, J., Picard, R. H., Roble, R. G., et al. (2009). Global ray tracing simulations of the SABER gravity wave climatology. *Journal of Geophysical Research*, *114*(D8), D08126. https://doi.org/10.1029/2008JD011214

Preusse, P., Ern, M., Eckermann, S. D., Warner, C. D., Picard, R. H., Knieling, P., et al. (2006). Tropopause to mesopause gravity waves in August: Measurement and modeling. *Journal of Atmospheric and Solar-terrestrial Physics*, *68*, 1730–1751. https://doi.org/10.1016/j.jastp.2005.10.019

Preusse, P., Ern, M., Grossmann, K. U., & Mergenthaler, J. L. (2004). Seasonal variations of gravity wave variance inferred from CLAES. In K. P. Schaefer, A. Comeron, M. R. Carleer, & R. H. Picard (Eds.), *Remote Sensing of Clouds and the Atmosphere VIII*. Proceedings of SPIE (Vol. 5235, pp. 288–297. https://doi.org/10.1117/12.514171

Randall, C. E., Carstens, J., France, J. A., Harvey, V. L., Hoffmann, L., Bailey, S. M., et al. (2017). New AIM/CIPS global observations of gravity waves near 50–55 km. *Geophysical Research Letters*, *44*(13), 7044–7052. https://doi.org/10.1002/2017GL073943

Sato, K., Watanabe, S., Kawatani, Y., Tomikawa, Y., Miyazaki, K., & Takahashi, M. (2009). On the origins of mesospheric gravity waves. *Geophysical Research Letters*, *36*(19), L19801. https://doi.org/10.1029/2009GL039908

Schmidt, H., Brasseur, G. P., Charron, M., Manzini, E., Giorgetta, M. A., Diehl, T., et al. (2006). The HAMMONIA chemistry climate model: Sensitivity of the mesopause region to the 11-year solar cycle and CO_2 doubling. *Journal of Climate*, *19*(16), 3903–3931. https://doi.org/10.1175/jcli3829.1

Thurairajah, B., Siskind, D. E., Bailey, S. M., Carstens, J. N., Russell, J. M., III, & Mlynczak, M. G. (2017). Oblique propagation of monsoon gravity waves during the northern hemisphere 2007 summer. *Journal of Geophysical Research: Atmospheres*, *122*(10), 5063–5075. https://doi.org/10.1002/2016JD026008

Trenberth, K. E., Stepaniak, D. P., & Caron, J. M. (2000). The global monsoon as seen through the divergent atmospheric circulation. *Journal of Climate*, *13*(22), 3969–3993. https://doi.org/10.1175/1520-0442(2000)013<3969:TGMAST>2.0.CO;2

Trinh, Q. T., Ern, M., Doornbos, E., Preusse, P., & Riese, M. (2018). Satellite observations of middle atmosphere-thermosphere vertical coupling by gravity waves. *Annales Geophysicae*, *36*(2), 425–444. https://doi.org/10.5194/angeo-36-425-2018

Trinh, Q. T., Kalisch, S., Preusse, P., Ern, M., Chun, H.-Y., Eckermann, S. D., et al. (2016). Tuning of a convective gravity wave source scheme based on HIRDLS observations. *Atmospheric Chemistry and Physics*, *16*(11), 7335–7356. https://doi.org/10.5194/acp-16-7335-2016

Truskowski, A. O., Forbes, J. M., Zhang, X., & Palo, S. E. (2014). New perspectives on thermosphere tides: 1. Lower thermosphere spectra and seasonal-latitudinal structures. *Earth, Planets and Space*, *66*, 136. https://doi.org/10.1186/s40623-014-0136-4

Vadas, S. L., & Liu, H.-L. (2009). Generation of large-scale gravity waves and neutral winds in the thermosphere from the dissipation of convectively generated gravity waves. *Journal of Geophysical Research*, *114*(A10), A10310. https://doi.org/10.1029/2009JA014108

Vadas, S. L., Liu, H.-L., & Lieberman, R. S. (2014). Numerical modeling of the global changes to the thermosphere and ionosphere from the dissipation of gravity waves from deep convection. *Journal of Geophysical Research: Space Physics*, *119*(9), 7762–7793. https://doi.org/10.1002/2014JA020280

Vincent, R. A., & Alexander, M. J. (2020). Balloon-borne observations of short vertical wavelength gravity waves and interaction with QBO winds. *Journal of Geophysical Research: Atmospheres*, *125*(15), e2020JD032779. https://doi.org/10.1029/2020JD032779

Wang, B., Ding, Q., & Liu, J. (2011). Concept of global monsoon. In C.-P. Chang, Y. Ding, N.-C. Liu, R. H. Johnson, B. Wang, & T. Yasunari (Eds.), *The Global Monsoon System, World Scientific Series on Asia-Pacific Weather and Climate eBook* (pp. 3–14). https://doi.org/10.1142/9789814343411_0001

Wang, B., & Ding, Q.-H. (2006). Changes in global monsoon precipitation over the past 56 years. *Geophysical Research Letters*, *33*(6), L06711. https://doi.org/10.1029/2005GL025347

Wright, C. J., & Gille, J. C. (2011). HIRDLS observations of gravity wave momentum fluxes over the monsoon regions. *Journal of Geophysical Research*, *116*(D12), D12103. https://doi.org/10.1029/2011JD015725

Wu, D. L., & Waters, J. W. (1996). Gravity-wave-scale temperature fluctuations seen by the UARS MLS. *Geophysical Research Letters*, *23*, 3289–3292. https://doi.org/10.1029/96gl02924

Yasui, R., Sato, K., & Tsutsumi, M. (2016). Seasonal and interannual variation of mesospheric gravity waves based on MF radar observations over 15 years at Syowa Station in the Antarctic. *Sola*, *12*(0), 46–50. https://doi.org/10.2151/sola.2016-010

Yiğit, E., & Medvedev, A. S. (2015). Internal wave coupling processes in Earth's atmosphere. *Advances in Space Research*, *55*(4), 983–1003. https://doi.org/10.1016/j.asr.2014.11.020

Yiğit, E., Medvedev, A. S., Aylward, A. D., Hartogh, P., & Harris, M. J. (2009). Modeling the effects of gravity wave momentum deposition on the general circulation above the turbopause. *Journal of Geophysical Research*, *114*(D7), D07101. https://doi.org/10.1029/2008JD011132